



ELSEVIER

Available online at www.sciencedirect.com

SCIENCE @ DIRECT®

Journal of Computational Physics xxx (2004) xxx–xxx

JOURNAL OF
COMPUTATIONAL
PHYSICSwww.elsevier.com/locate/jcp

An efficient model for three-dimensional surface wave simulations Part I: Free space problems

Dorian Fructus, Didier Clamond, John Grue *, Øyvind Kristiansen

Mechanics Division, Department of Mathematics, University of Oslo, P.O. Box 1053, Blindern, 0316 Oslo, Norway

Received 1 July 2004; received in revised form 7 July 2004; accepted 29 November 2004

Abstract

An efficient numerical scheme for simulations of fully nonlinear non-breaking surface water waves in 3D is presented. The water depth is either shallow, finite or infinite. The method is based on a fast, rapidly converging, iterative algorithm to compute the Dirichlet to Neumann operator. This is evaluated by expanding the operator as a sum of global convolution terms and local integrals with kernels that decay quickly in space. The global terms are computed very quickly via FFT. The local terms are evaluated by numerical integration. Analytical integration of the linear part of the prognostic equations in Fourier space is obtained to machine precision. The remaining nonlinear components are integrated forward in time using an RK-scheme combined with a special step size control technique. This yields a very stable and accurate time marching procedure. Zeros-padding in the spectral space represents the anti-aliasing strategy. The method requires no smoothing. Illustration through examples show that the total energy is well conserved during the numerical simulations. The scheme is stable and accurate, even for very long time simulations of very steep wave events. The scheme is easily parallelizable. It propagates for example a Stokes wave of slope 0.2985 with a phase shift error of about 0.3° after 1000 periods of propagation.

© 2004 Published by Elsevier Inc.

Keywords: Surface waves; Fully nonlinear; Three-dimensional; Boundary integral formulation; Pseudo-spectral method; Rapid Dirichlet to Neumann operator

* Corresponding author. Tel.: +47 2285 5839; fax: +47 2285 4349.

E-mail addresses: dorianf@math.uio.no (D. Fructus), didier@math.uio.no (D. Clamond), johng@math.uio.no (J. Grue), oyvinkri@math.uio.no (Ø. Kristiansen).

27 1. Introduction

28 The rapidly increasing computer power enables computations that are significantly more advanced than
29 until recently were possible. There are problems that are so demanding that they will not be solved in the
30 near future by only increasing the hardware capabilities, however. To solve such types of problems, it is also
31 necessary to improve the numerical algorithms reducing substantially the amount of calculations. Direct
32 simulations of three-dimensional surface water waves is one example. Wave propagation over long time
33 in large domains is a very demanding numerical task, that cannot be tackled by the brute force approach.
34 This paper describes a novel efficient numerical method for fully nonlinear three-dimensional surface wave
35 simulations. The method is very efficient from a computational point of view and is suitable for simulations
36 using parallel computers.

37 Computations of very steep ocean waves represents an important challenge. The evolution of long wave
38 fields and the action of instability mechanisms have been focused in several studies following the pioneering
39 works of Benjamin and Feir [2] and Zakharov [40]. Reviews of the advances can be found in [15,39]. Recent
40 studies focus on instabilities and the formation of very big waves at sea [12,16,22,27,33]. The effect of non-
41 linear four-wave interactions on the formation of freak waves was studied by Janssen [21] using the NLS
42 and the Zakharov equations. How a wave spectrum of a sea relaxes toward stationary state was recently
43 studied by Dysthe et al. [13] using extended NLS equations in two horizontal dimensions.

44 Various approaches have been derived to solve exactly or approximately the surface wave problems
45 (see [9,15,34] for reviews). These methods can be divided into three categories: the simplified equations,
46 the high-order spectral methods and the boundary integral formulations. The oldest and simplest models
47 are based on equations as, e.g. the nonlinear Schrödinger equation or extensions of this equation [12,33].
48 These equations are easily and quickly solved numerically, and for some of them even analytically. The
49 ranges of validity are limited and they cannot be used for steep waves or long time simulations, however.
50 High-order spectral methods are based on Taylor expansions [8,11,37]. They are computationally efficient
51 when the series converge, meaning that the waves must not be too steep. For high-order approximations,
52 the methods involve high-order derivatives and nonlinearities. The schemes then become inaccurate and
53 numerically unstable. For highly nonlinear waves these methods do not converge. In practice, few terms
54 are used. If rewritten in the Fourier space, these equations, with low-order expansions, include the
55 Zakharov equation [40]. Other methods for three-dimensional water wave simulations also exist (see
56 [1,19]).

57 The request for an improved understanding of the formation of very big waves motivated us to initiate a
58 fully nonlinear modeling of the phenomenon in three dimensions. It is important that the method is rapid
59 and the time integration accurate. This is fundamental, since realistic wave analysis typically is carried out
60 for large physical domains and long time. A fully nonlinear modeling was requested by the recent ISSC-
61 report [20], for example.

62 Our computational strategy is based on an integral equation formulation and extensive use of Fourier
63 transform. This solves the Laplace equation in the fluid domain, expressing the normal velocity at the free
64 surface in terms of the potential at the free surface and the wave elevation (the Dirichlet to Neumann oper-
65 ator). The dominant part of the solution is global and is obtained by fast Fourier transform (FFT). The
66 remaining part is highly nonlinear and have integrals with kernels that decay quickly in the space coordi-
67 nate. The iterative method is so rapidly convergent that one iteration is sufficient for most practical appli-
68 cations. In such cases the method is explicit. The method follows the mathematical formulae that were
69 derived in Clamond and Grue [6] for an infinitely deep fluid in three dimensions and generalized to single
70 and two layer motion with finite depths in three dimensions in Grue [17]. So far, the method was neither
71 implemented nor tested out in practical (3D) computations.

72 This paper communicates important extensions of the previous publications by Clamond and Grue
73 [6] and by Grue [17] on three main points. These include, firstly, an enhanced subdivision between

74 the global and local contributions to the inversion of the Laplace equation solver. We find that in the
75 three-dimensional computational scheme, it is highly useful to include one more term in the global Fou-
76 rier inversion of the integral equation, as compared to the two-dimensional procedure. Further, the con-
77 tributions resulting from the imaging through the sea floor are enhanced, as compared to the initial
78 formulae given in Grue [17]. The added terms in the global evaluation of the Dirichlet to Neumann
79 operator are evaluated by FFT which significantly speeds up the performance of the scheme in 3D.
80 The additions to the Fourier inversion part share the beauty of analyticity which is ideal for potential
81 manipulations.

82 Secondly, how to perform a highly accurate time integration of the three-dimensional problem is ad-
83 dressed here for the first time. This is a nontrivial extension of the time integrator in Clamond and Grue
84 in two dimensions. The conservative form of the equations differs from the two-dimensional case, see
85 Eqs. (20) and (21) below. Further, another decomposition of the dynamical boundary condition is em-
86 ployed in 3D, where the formula also includes new terms as compared to 2D. This substantially modifies
87 the computational strategy.

88 Finally, the implementation of the method is tested and documented more systematically than what
89 has been previously done. The detailed implementation of the de-aliasing technique for the products
90 in three dimensions is highlighted. The accuracy is mainly governed by two parameters: TOL and ITER.
91 The former sets the tolerance of the time-integrator scheme and is actively used in the step-size control.
92 The parameter ITER determines the number of iterations in the inversion of the Laplace equation solver.
93 Numerical experiments with Stokes waves shows that using ITER = 1 and TOL = 10^{-8} , i.e., in practice an
94 explicit scheme, leads to highly accurate results, with an error in the wave phase of 75° after 1000 periods
95 of propagation, conserving the energy, however. This phase error is returned to zero upon reversal of the
96 time stepping. Further tests, using an enhanced resolution, document that using ITER = 3 and TOL = 10^{-8}
97 reduces the error in the wave phase to 0.3° after 1000 periods of propagation, returning the wave phase
98 to 0° upon reversal of the time stepping. The same result is obtained using ITER = 5 and TOL = 10^{-8}
99 meaning that only very few iterations are required still keeping a highly accurate and energy conserving
100 scheme.

101 This paper provides a complete description of the mathematical method and its numerical implementa-
102 tion in three dimensions. The performance of the method is illustrated in several examples. The description
103 is divided into this part I, focussing on wave motion in an infinite domain (using periodic boundary con-
104 ditions). A complementary part II [5] describes a fully nonlinear wave generation procedure and a novel
105 efficient wave damping strategy, with zero reflection.

106 This paper (part I) is organized as follows: Section 2 of the paper describes the prognostic equations (ob-
107 tained from the kinematic and dynamic boundary conditions) and the integral equation solving the Laplace
108 equation in the fluid domain. Reorganization and inversion of the integral equation using Fourier trans-
109 form leads to a rapid method for the normal velocity at the free surface. Section 3 describes the numerical
110 algorithms, the anti-aliasing technique, how to compute the global contributions from the integral equation
111 and how to evaluate the local contributions that are fast-decaying in space. The time stepping method is
112 further described. Section 4 describes the numerical tests, including integration of a progressive Stokes wave
113 10^3 periods forward in time, and return, a progressive solitary wave, and highly nonlinear evolution of cres-
114 cent wave patterns. Finally, Section 5 is concluding remarks.

115 2. Mathematical formulation

116 We consider three-dimensional irrotational wave motion at the surface of a homogeneous incompress-
117 ible fluid over a horizontal impermeable bottom.

118 2.1. Equations in the physical space

119 Let $\mathbf{x} = (x_1, x_2)$ be the horizontal Cartesian coordinates, y the upward vertical coordinate and t the time.
 120 $y = \eta(\mathbf{x}, t)$ determines the surface elevation (with $y = 0$ the level at rest) and $y = -h$ the level of the imper-
 121 meable horizontal bottom. Let $\vec{v} = (\mathbf{u}, v)$ be the velocity field, where $\mathbf{u} = (u_1, u_2)$ and v are the horizontal and
 122 vertical velocities, so that $\vec{v} = \text{grad } \phi$, $\mathbf{u} = \nabla \phi$ and $v = \phi_y$, where ϕ denotes the velocity potential and ∇ the
 123 horizontal gradient. We denote with ‘tildes’ the quantities at the free surface, e.g. $\tilde{\phi}(\mathbf{x}, t) =$
 124 $\phi(\mathbf{x}, y = \eta(\mathbf{x}, t), t)$. Note that $\tilde{\mathbf{u}} = \nabla \tilde{\phi}$ differs from $\nabla \phi = \tilde{\mathbf{u}} + \tilde{v} \nabla \eta$. At the free surface, $\tilde{\mathbf{u}}$ and \tilde{v} are expressed
 125 by:

$$\tilde{\mathbf{u}} = \frac{\nabla \tilde{\phi} - V \nabla \eta + (\nabla \eta \times \nabla \tilde{\phi}) \times \nabla \eta}{1 + |\nabla \eta|^2}, \quad \tilde{v} = \frac{V + \nabla \eta \cdot \nabla \tilde{\phi}}{1 + |\nabla \eta|^2}, \quad (1)$$

129 where $V = \partial \phi / \partial n \sqrt{1 + |\nabla \eta|^2}$ and \vec{n} denotes the outward normal of unit length at the free surface.

130 At the free surface, the pressure p (per unit mass) is either zero, or balances the effect of a surface tension
 131 (if taken into account), a generating pressure \tilde{p}_G (i.e., a pneumatic wavemaker) and a dissipative pressure \tilde{p}_D
 132 (i.e., a wave absorber). The free surface is generally material. For immaterial surfaces, one can also consider
 133 a prescribed vertical velocity \tilde{v}_D at the surface ($\tilde{v}_D = 0$ for a material surface). The velocity \tilde{v}_D can be used to
 134 introduce a damping effect in order to absorb waves (similar to the damping pressure \tilde{p}_D). Efficient proce-
 135 dures of wave generation and wave damping are addressed in the accompanying paper, Part II [5].

136 The kinematic and dynamic conditions at the surface can be conveniently written:

$$\eta_t - V = \tilde{v}_D, \quad (2)$$

$$\tilde{\phi}_t + g\eta + \frac{1}{2} \tilde{\mathbf{u}} \cdot \nabla \tilde{\phi} - \frac{1}{2} \tilde{v} V = \sigma \nabla \cdot \left[\frac{\nabla \eta}{\sqrt{1 + |\nabla \eta|^2}} \right] - \tilde{p}_G - \tilde{p}_D, \quad (3)$$

143 where g being the acceleration of gravity and σ the (constant) surface tension coefficient. The generating
 144 pressure \tilde{p}_G , the damping pressure \tilde{p}_D and velocity \tilde{v}_D are not used in Part I. They will be defined in Part
 145 II of the paper. In the numerical examples below we shall take $\tilde{p}_G = \tilde{p}_D = \tilde{v}_D = \sigma = 0$.

146 The solution of the Laplace equation (resulting from incompressibility and irrotationality) provides a
 147 relation between the (unknown) normal velocity at the surface, defined through V below Eq. (1), and
 148 the (known) quantities $\tilde{\phi}$ and η at the surface (and their spacial derivatives). This relation defines an oper-
 149 ator which produces the Neumann data V from the Dirichlet data $\tilde{\phi}$. This operator is often referred to as
 150 the Dirichlet to Neumann operator.

151 The Laplace equation, together with the bottom impermeability, is solved exactly by means of a Green
 152 function and the method of images ([6, Section 6]; [17, Section 6]), i.e.

$$\int_S \left(\frac{1}{\tilde{r}} + \frac{1}{\tilde{r}_B} \right) \frac{\partial \tilde{\phi}'}{\partial n'} dS' = 2\pi \tilde{\phi} + \int_S \tilde{\phi}' \frac{\partial}{\partial n} \left(\frac{1}{\tilde{r}} + \frac{1}{\tilde{r}_B} \right) dS', \quad (4)$$

156 where $\tilde{\phi} = \tilde{\phi}(\mathbf{x}, t)$, $\tilde{\phi}' = \tilde{\phi}(\mathbf{x}', t)$, $r^2 = R^2 + (y' - y)^2$ and $r_B^2 = R^2 + (y' + y + 2h)^2$.

157 Here, $R = |\mathbf{R}|$ denotes the horizontal distance between the field point and the source point, where
 158 $\mathbf{R} = \mathbf{x}' - \mathbf{x}$. In (4) S denotes the instantaneous free surface of the fluid.

159 In the paper [6], Clamond and Grue introduced the variable $D = [\eta(\mathbf{x}', t) - \eta(\mathbf{x}, t)]/R = [\eta' - \eta]/R$. Note
 160 that $D \sim R^{-1}$ as $R \rightarrow \infty$ and $D \rightarrow \partial \eta / \partial R$ as $R \rightarrow 0$. Correspondingly, a variable D_B is introduced by

161 $D_B = [\eta' + \eta]/R_B$ where $R_B = \sqrt{R^2 + 4h^2}$. For non-overturning surfaces with $dS' = \sqrt{1 + |\nabla' \eta|^2} dx'_1 dx'_2$,

162 the integral equation may be expressed in the form

$$\begin{aligned} & \int \frac{V'}{(1+D^2)^{1/2}} \frac{d\mathbf{x}'}{R} + \int \frac{V'}{(1+4hD_B R_B^{-1} + D_B^2)^{1/2}} \frac{d\mathbf{x}'}{R_B} \\ & = 2\pi\tilde{\phi} + \int \frac{\tilde{\phi}'(\mathbf{R} \cdot \nabla' \eta' - \eta' + \eta)}{(1+D^2)^{3/2}} \frac{d\mathbf{x}'}{R^3} + \int \frac{\tilde{\phi}'(\mathbf{R} \cdot \nabla' \eta' - \eta' - \eta - 2h)}{(1+4hD_B R_B^{-1} + D_B^2)^{3/2}} \frac{d\mathbf{x}'}{R_B^3}, \end{aligned} \quad (5)$$

166 where the following convenient brief notation is used:

$$\int \bullet d\mathbf{x}' \equiv \int_{-\infty}^{\infty} \int_{-\infty}^{\infty} \bullet dx'_1 dx'_2. \quad (6)$$

169 2.2. Reformulation of the boundary integrals

170 The direct numerical computation of V from the boundary integrals in (5) is demanding and not suitable
 171 for large domains and long time simulations. A more suitable formulation is derived rewriting the lowest-
 172 order nonlinear terms as convolutions, the remaining integrals having rapidly decaying kernels allowing
 173 truncated integrations [6]. For simplicity, we present here the deep water case only ($h = \infty$). The corre-
 174 sponding expansion for finite depth is given in Appendix A.

175 Following [6] we first exploit that

$$\frac{\mathbf{R} \cdot \nabla' \eta'}{R^3} - \frac{\eta' - \eta}{R^3} = -\nabla' \cdot \left[(\eta' - \eta) \nabla' \frac{1}{R} \right]. \quad (7)$$

178 Then, by application of Gauss theorem, we may partially rewrite the corresponding integral in (5). The
 179 modified and reorganized version of the equation reads (with $h = \infty$, see [6])

$$\begin{aligned} \int V' R^{-1} d\mathbf{x}' & = 2\pi\tilde{\phi} + \int (\eta' - \eta) \nabla' \tilde{\phi}' \cdot \nabla' R^{-1} d\mathbf{x}' + \int V' R^{-1} \left[1 - (1+D^2)^{-1/2} \right] d\mathbf{x}' \\ & \quad + \int \tilde{\phi}' \left[1 - (1+D^2)^{-3/2} \right] \nabla' \cdot [(\eta' - \eta) \nabla' R^{-1}] d\mathbf{x}'. \end{aligned} \quad (8)$$

182 A decomposition $V = V_1 + V_2 + V_3 + V_4$ is introduced, where:

$$\int V'_1 R^{-1} d\mathbf{x}' = 2\pi\tilde{\phi}, \quad (9)$$

$$\int V'_2 R^{-1} d\mathbf{x}' = \int (\eta' - \eta) \nabla' \tilde{\phi}' \cdot \nabla' R^{-1} d\mathbf{x}', \quad (10)$$

$$\int V'_3 R^{-1} d\mathbf{x}' = \int \tilde{\phi}' \left[1 - (1+D^2)^{-3/2} \right] \nabla' \cdot [(\eta' - \eta) \nabla' R^{-1}] d\mathbf{x}', \quad (11)$$

$$\int V'_4 R^{-1} d\mathbf{x}' = \int V' R^{-1} \left[1 - (1+D^2)^{-1/2} \right] d\mathbf{x}'. \quad (12)$$

195 Fourier transform is then applied to invert the equations (for the unknowns V_1, V_2, V_3 and V_4). For the left
 196 hand sides of (9)–(12) we get

$$\mathcal{F} \left\{ \int V'_j R^{-1} d\mathbf{x}' \right\} = 2\pi k^{-1} \int V'_j e^{-ik \cdot \mathbf{x}'} d\mathbf{x}' = 2\pi k^{-1} \hat{V}_j, \quad (13)$$

199 where the Fourier transform \mathcal{F} is defined as:

6

D. Fructus et al. / Journal of Computational Physics xxx (2004) xxx–xxx

$$\hat{\phi}(\mathbf{k}, t) = \mathcal{F}\{\tilde{\phi}\} = \int \tilde{\phi}(\mathbf{x}, t) e^{-i\mathbf{k}\cdot\mathbf{x}} d\mathbf{x},$$

$$\tilde{\phi}(\mathbf{x}, t) = \mathcal{F}^{-1}\{\hat{\phi}\} = \frac{1}{4\pi^2} \int \hat{\phi}(\mathbf{k}, t) e^{i\mathbf{k}\cdot\mathbf{x}} d\mathbf{k},$$

204 where $\mathbf{k} = (k_1, k_2)$ denotes the wavenumber, and $k = |\mathbf{k}|$. We have exploited that $\mathcal{F}\{R^{-1}\} = 2\pi k^{-1} e^{-i\mathbf{k}\cdot\mathbf{x}'}$. The
 205 transformed Eq. (9) becomes $\hat{V}_1 = k\hat{\phi}$ and, similarly, for the other terms we obtain ([6, Section 6]):

$$\hat{V}_2 = -k\mathcal{F}\{\eta V_1\} - i\mathbf{k} \cdot \mathcal{F}\{\eta \nabla \tilde{\phi}\}, \quad (14)$$

$$2\pi\hat{V}_3 = k\mathcal{F}\left\{\int \tilde{\phi}' \left[1 - (1 + D^2)^{-3/2}\right] \nabla' \cdot [(\eta' - \eta) \nabla' R^{-1}] d\mathbf{x}'\right\}, \quad (15)$$

$$2\pi\hat{V}_4 = k\mathcal{F}\left\{\int V' R^{-1} \left[1 - (1 + D^2)^{-1/2}\right] d\mathbf{x}'\right\}. \quad (16)$$

214 In finite depth computations, a corresponding set of equations results from (A.2), see Appendix A.

215 2.3. Global and local integration

216 In [6] only the quadratic terms (\hat{V}_2) were written as convolutions. We push here this expansion further in
 217 writing also a part of the cubic term as convolutions (\hat{V}_4). This allows us to write the integral (16) as a sum
 218 of convolutions, which are computed via Fourier transform, plus an integral with a kernel that decays (even
 219 more) quickly

$$2\pi\hat{V}_4 = k\mathcal{F}\left\{\int V' R^{-1} \frac{1}{2} D^2 d\mathbf{x}'\right\} + k\mathcal{F}\left\{\int V' R^{-1} \left[1 - \frac{1}{2} D^2 - (1 + D^2)^{-1/2}\right] d\mathbf{x}'\right\}. \quad (17)$$

223 The former integral is easily obtained by convolutions, i.e.

$$k\mathcal{F}\left\{\int V' R^{-1} \frac{1}{2} D^2 d\mathbf{x}'\right\} = -\pi k \mathcal{F}\{\eta^2 \mathcal{F}^{-1}\{k\mathcal{F}\{V\}\}\} - 2\eta \mathcal{F}^{-1}\{k\mathcal{F}\{\eta V\}\} + \mathcal{F}^{-1}\{k\mathcal{F}\{\eta^2 V\}\}.$$

226 The kernels of the inner integrals of (15) and of the second term on the right hand side of (17) decay like
 227 R^{-4} and R^{-5} , respectively. These integrals may be evaluated over a very limited region of the \mathbf{x} -plane, still
 228 keeping high accuracy.

229 While V_1 , V_2 , and V_3 are determined by known functions at the free surface, V_4 is determined implic-
 230 itly. The latter is computed iteratively using an iteration procedure that may be continued until a de-
 231 sired accuracy is achieved. The number of iterations is in the code determined by the parameter ITER
 232 (see Section 3.2 below). In many practical computations one iteration (ITER = 1) is sufficient, however,
 233 i.e., we replace V by $V_1 + V_2 + V_3$ in the right-hand side of (17). In this case the inversion procedure of
 234 the Laplace equation is explicit. The simulations presented in Section 4 below show that an enhanced
 235 accuracy is obtained if three iterations (using ITER = 3) are performed. This is important if the time
 236 simulations are very long or of high complexity. Comparisons using ITER = 1, 3 and 5 show that the
 237 two latter give the same accuracy, while ITER = 1 gives an excellent prediction, which can be refined,
 238 however.

239 The solution of the Laplace equation presented here can be viewed as a “hybrid” between the expansion
 240 method [8,11,37] and the boundary integral method [10,23], taking advantage of the features of both for-
 241 mulations: speed and accuracy.

242 2.4. Remarks

243 In cases when $D^2 < 1$, the term $1 - (1 + D^2)^{-1/2}$ has a convergent series expansion of the form

$$1 - (1 + D^2)^{-1/2} = \frac{1}{2}D^2 - \frac{3}{8}D^4 + \frac{5}{16}D^6 + \dots \quad (D^2 < 1). \quad (18)$$

246 This infinite expansion can formally be used to rewrite the integral V_4 in the form of a sum of convolutions
 247 only. Hence, after functional iterations, one obtains an explicit expression for V which, after some analyt-
 248 ical manipulations, reduces to the expansion of the Dirichlet–Neumann operator due to Craig and Sulem
 249 [8]. However, this method suffers of several drawbacks (see also comments in Section 2.5 below):

- 250 (i) The series converges for $D^2 < 1$ only. There are physical situations where $|D|$ is locally close to one for
 251 non-breaking waves.
- 252 (ii) Even if the series does converge, the convergence is very slow, except for very small $|D|$. A significant
 253 gain of accuracy can therefore be expected only at the expense of considerable computations.
- 254 (iii) Since calculations are performed with finite precision arithmetics, the gain expected from higher trun-
 255 cations is annihilated by a large accumulation of round-off errors. Thus, even for small $|D|$, the use-
 256 fulness of higher-order expansions is limited [31].
- 257 (iv) The convolution terms involve high-order derivatives that increase with the order of truncation. Com-
 258 putations of high-order derivatives are numerically unstable. On the other hand, computations of inte-
 259 grals have natural smoothing effects. Note that in the two-dimensional version of the model as it is
 260 implemented in [6], only the quadratic terms (\hat{V}_2) can be rewritten as convolutions keeping the scheme
 261 stable. The method is therefore better conditioned in three than in two dimensions.
- 262 (v) Another inconvenience with the convolution terms is their ill-conditioning due to cancellations. This
 263 puts additional restrictions on the efficiency of the expansion methods.
- 264 (vi) Finally, it turns out that expansions methods are competitive only at low-order truncations, i.e., to
 265 simulate waves with small steepnesses over relatively short periods of time.

266 If the computation of V is limited to the convolution terms, our scheme is comparable to the classical
 267 Zakharov equation [40]. This is therefore a decently accurate approximation. Thus, very fast investigations
 268 can be performed computing $V_1 + V_2 + V_4$ only (V_4 being computed replacing V by $V_1 + V_2$ in the right
 269 hand side of (17) without the integral), and when interesting results are obtained, the computations are re-
 270 done with the entire solution.

272 In summary, our main conclusion is that the term $1 - (1 + D^2)^{-1/2}$ is best divided into the sum

$$1 - (1 + D^2)^{-1/2} = \frac{1}{2}D^2 - \left[(1 + D^2)^{-1/2} - 1 + \frac{1}{2}D^2 \right],$$

275 where the first term ($\frac{1}{2}D^2$) contributes to a global evaluation, and the second to a local, truncated integra-
 276 tion. This division is found to be insensitive to the magnitude of $|D|$. If $|D|$ is moderately small, the second
 277 term is correspondingly small and may be neglected.

278 An alternative is to split the term into

$$\frac{1}{2}D^2 - \frac{3}{8}D^4 - \left[(1 + D^2)^{-1/2} - 1 + \frac{1}{2}D^2 - \frac{3}{8}D^4 \right]$$

281 including also $(-3/8)D^4$ in the global evaluation, and the remaining part as an even stronger local, trun-
 282 cated integration. This strategy has been tested and found to lead to a numerically unstable procedure.

283 We have found that it is important to keep terms up to cubic appearance (due to the free surface con-
 284 tribution), but stop a further expansion of the Dirichlet to Neumann operator. With this, we derive a highly
 285 efficient anti-aliased scheme, see Section 3.1 below. For images through the bottom (finite depth contribu-

286 tion) higher order convolutions are still effective, because the Fourier transform typically then involves a
287 factor e^{-2kh} , contributing to a strong reduction of the energy at high wavenumbers.

288 2.5. Further comments

289 While standard expansion methods suffer from significant ill-conditioning problems, alternative pertur-
290 bative approaches for problems in 2D, leading to a stable evaluation of the Dirichlet to Neumann operator,
291 are studied by Nicholls and Reitich [26]. A detailed stability analysis was recently presented by Hou and
292 Zhang [19] for the point vortex method for 2D water waves, adding stabilizing terms to the boundary inte-
293 gral method that exactly cancels a destabilizing term produced by using a point vortex method. Such strat-
294 egies were not required with the present, non-perturbative formulation.

295 3. Numerical algorithms

296 The computational domain is rectangular, periodic in both directions and discretized with constant steps
297 $\Delta \mathbf{x} = (\Delta x_1, \Delta x_2)$ over $2N = 2(N_1, N_2)$ nodes. $\pi/\Delta x_i$ is thus the highest wavenumber (the Nyquist frequency) in
298 the i th direction.

299 Simulations of non-periodic problems are achieved embedding the physical domain into a larger periodic
300 box and using absorbing boundary conditions described in the Part II [5].

301 All the linear operations (e.g. differentiation) are computed in Fourier space and all the nonlinear ones in
302 physical space. The transfers between physical and spectral space are obtained by FFT algorithms. The
303 computations of the nonlinear terms require special care in order to avoid aliasing. We emphasize that
304 the anti-aliasing technique explained below is the only method used to avoid numerical instabilities: we
305 do not use, e.g. smoothing interpolations, regridding, artificial numerical viscosity, etc.

306 3.1. Anti-aliasing technique

307 For the numerical stability, it is crucial to compute the nonlinear terms free of aliasing errors ([3,4], Sec-
308 tion 3.2).

309 The product between two discrete functions in physical space corresponds to a circular convolution in
310 Fourier space (the spectra are periodic). De-aliased computations can be performed extending the spectra
311 by zeros padding ([4], Section 3.2). The spectra must be extended by (at least) a factor of three-half for qua-
312 dratic nonlinearities. Similarly, extensions by a factor four-half is required for cubic nonlinearities, by a fac-
313 tor of five-half for quartic nonlinearities, etc. This method becomes expensive, in terms of computational
314 time and memory, for high-order nonlinearities. Instead, we apply repeatedly the *four-half rule*, setting
315 to zero the extra wavenumbers each time a double or triple product is performed.

316 Note that, for example, it is not exactly equivalent to compute f^4 with the five-half rule and to compute
317 $f^2 \times f^2$ applying twice the three-half rule (or to compute $f^3 \times f$ applying first the four-half rule and then the
318 three-half rule). However, the Fourier spectra of regular functions being exponentially decaying, the error
319 induced by repeated applications of the three-half rule as $(f^2)^2$ is comparable to the round-off error, if the
320 discretization of f is sufficiently refined.

321 3.2. Computation of V

322 The integrals involved in V_3 and V_4 are truncated for $\mathbf{x}' \in [\mathbf{x} - \lambda; \mathbf{x} + \lambda]$, λ being given a priori. Since the
323 kernels of the integrals are decaying rapidly λ can be taken much smaller than the size of the computational
324 box. In practice λ is chosen as one characteristic wavelength (e.g. the peak frequency of a JONSWAP spec-

trum), which is sufficient for most applications. The effect of truncation was studied in detail in [6] for the two-dimensional case. In the present three-dimensional extension of the method, the kernels decay faster than their two-dimensional counterparts, justifying the truncation over one typical wavelength. Note that the truncation depends on the wave field characteristics and not on the size of the computational domain. This means that the computational time increases linearly with the domain size, and not quadratically (or even worse) as in other methods.

The implicit term in V_4 is computed applying simple functional iterations. The number of iterations used for its evaluation is `ITER`. One iteration is often sufficient in practice. Of course, the required number of iterations `ITER` depends on the phenomenon studied and on the desired accuracy.

The domain is discretized with constant steps and the integrals are computed using the trapezoidal rule. According to the Euler–MacLaurin formula, this provides a very accurate approximation. To avoid explicit treatment of apparent singularities at $\mathbf{x}' = \mathbf{x}$, the integrands are evaluated at the nodes $\mathbf{x}_j = (j + \frac{1}{2})\Delta\mathbf{x}$, and shifted back to the regular nodes via Fourier interpolations (requiring two FFTs).

Note that the computation of the regular integrals is, by essence, easily parallelizable. The implementation is done in Fortran 90. This allows the use of multiprocessor systems, either using shared memory parallel systems (SMP), dispatched memory parallel systems (DMP) or a combination of both (hybrid solution). This is exploited by dividing the physical domain where the integrals have to be computed into sub-domains. A given sub-domain is then resolved by a single node (which may itself be a SMP system if the machine used is of hybrid type). The computation of the integrals is the more demanding part. The execution time is therefore (roughly) divided by the number of processors available. The procedure is fast, and becomes particularly interesting when considering large domains where the use of hybrid machines can really be exploited.

3.3. Time stepping

Extracting the linear parts of (2) and (3) and taking their Fourier transforms, these equations are rewritten into the skew-symmetric form

$$\hat{F}_t + \check{A}\hat{F} + \hat{R} = \hat{N}, \quad (19)$$

where:

$$\hat{R} = \begin{pmatrix} 0 \\ \frac{k\omega}{g}\hat{p}_G \end{pmatrix}, \quad \hat{F} = \begin{pmatrix} k\hat{\eta} \\ \frac{k\omega}{g}\hat{\phi} \end{pmatrix}, \quad \check{A} = \begin{bmatrix} 0 & -\omega \\ \omega & 0 \end{bmatrix}, \quad (20)$$

$$\hat{N} = \begin{pmatrix} k\mathcal{F}\{V - V_1 + \tilde{v}_D\} \\ \frac{k\omega}{2g}\mathcal{F}\left\{\tilde{v}V - \tilde{\mathbf{u}} \cdot \nabla\tilde{\phi} + 2\sigma\nabla \cdot \left[\frac{(\sqrt{1+|\nabla\eta|^2}-1)\nabla\eta}{\sqrt{1+|\nabla\eta|^2}}\right]\right\} - \frac{k\omega}{g}\hat{p}_D \end{pmatrix}, \quad (21)$$

and $g = g + \sigma k^2$ and $\omega = \sqrt{gk \tanh kh}$. Eq. (19) form a conservative system of equations (if $\tilde{p}_G = \tilde{p}_D = \tilde{v}_D = 0$) for the pair of dimensionless dependent variables $k\hat{\eta}$ and $k\omega\hat{\phi}/g$.

The temporal resolution of such a system is very stiff for large ω , and the time step must therefore be very small. To avoid this problem, it is advantageous to introduce the change of dependent function (integrating factor [3]):

$$\hat{F}(\mathbf{k}, t) = \exp[\check{A}(t_0 - t)]\hat{G}(\mathbf{k}, t) - \int_{t_0}^t \exp[\check{A}(t' - t)]\hat{R}(\mathbf{k}, t') dt', \quad (22)$$

$$\hat{G}(\mathbf{k}, t) = \exp[\check{A}(t - t_0)]\hat{F}(\mathbf{k}, t) + \int_{t_0}^t \exp[\check{A}(t' - t_0)]\hat{R}(\mathbf{k}, t') dt', \quad (23)$$

369 which yields the equation

$$\hat{G}_t = \exp[\tilde{A}(t - t_0)]\hat{N}, \quad \hat{G}(\mathbf{k}, t_0) = \hat{F}(\mathbf{k}, t_0). \quad (24)$$

373 The nonlinear system (24) is then solved via a six-stages fifth-order Runge–Kutta scheme with an embedded
 374 fourth-order scheme for the time stepping control (Hairer and Wanner [18]). Since water wave problems are
 375 numerically very stiff, a stabilization of the time step is achieved by a special “PI step size control” (see [18,
 376 IV Section 2]). Numerical tests have shown that such a stabilization technique yields a substantial improve-
 377 ment to the method. We denote by `TOL` the tolerance required for the time integrator scheme.

378 Due to the analytic integration of the linear part, the scheme is unconditionally linearly stable and exact.
 379 For the temporal integration of the nonlinear remaining equation, many integrators are possible (including
 380 multiple steps, Taylor expansions, nonlinear, symplectic and hybrid schemes). We have found that the
 381 scheme above represents a very good compromise between: ease of implementation, speed, memory require-
 382 ment, stability, accuracy and conservation of invariants.

383 We note that if we now neglect the right hand side of (24) (no dissipation nor nonlinearities, $\hat{N} = 0$),
 384 $\hat{G}(\mathbf{k}, t) = \hat{F}(\mathbf{k}, t_0)$. This leads to the following linear solution:

$$\begin{aligned} \hat{\eta}(\mathbf{k}, t) &= \hat{\eta}_0 \cos \omega(t - t_0) + \frac{\omega}{g} \hat{\phi}_0 \sin \omega(t - t_0) - \frac{\omega}{g} \int_{t_0}^t \hat{p}_G(\mathbf{k}, t') \sin \omega(t - t') dt', \\ \hat{\phi}(\mathbf{k}, t) &= \hat{\phi}_0 \cos \omega(t - t_0) - \frac{g}{\omega} \hat{\eta}_0 \sin \omega(t - t_0) - \int_{t_0}^t \hat{p}_G(\mathbf{k}, t') \cos \omega(t - t') dt', \end{aligned} \quad (25)$$

387 where $\hat{\eta}_0 = \hat{\eta}(\mathbf{k}, t_0)$, $\hat{\phi}_0 = \hat{\phi}(\mathbf{k}, t_0)$. Once the term $\hat{p}_G(\mathbf{k}, t)$ is defined, one can explicitly express analytically
 388 the linear solution (some explicit solutions for different functions $\hat{p}_G(\mathbf{k}, t)$ are given in the part II [5]).

389 4. Numerical tests

390 We have chosen three different test cases relevant to typical problems of surface gravity waves. We pres-
 391 ent first two sets of simulations of long-crested progressive waves in deep and shallow water (i.e., a Stokes
 392 wave and a solitary wave). We also illustrate the method with a purely unsteady three-dimensional appli-
 393 cation (horse shoe) for which accurate experimental data are available. Our primary goal is to illustrate the
 394 method and to show that the procedure is fast, robust and very accurate.

395 The accuracy of the simulations are governed by the two parameters: `TOL` and `ITER`, where the former is
 396 used in the step-size control, and the latter determines the number of iterations in the inversion of the La-
 397 place equation solver.

398 4.1. Progressive Stokes wave

399 We first consider the propagation in deep water of an exact Stokes wave of steepness $ak = 0.2985$ (a the
 400 half wave height and k the wavenumber). The initial condition (i.e., at $t = 0$) for the free surface elevation η
 401 and the potential at the surface ϕ are obtained from Fenton’s exact numerical solver [14]. The computa-
 402 tional domain is quadratic and includes two wavelengths in each horizontal direction. It is discretized over
 403 64×64 collocation points, meaning that the first seven harmonics of the Stokes wave are resolved.

404 In an attempt to evaluate the accuracy of both the temporal integrator scheme and of the evaluation
 405 procedure of V , we assess the problem of reversibility of the solution. We study the evolution of the
 406 phase shift $\Delta\varphi$ and of the total energy (defined by $2E = \int (\eta_t \dot{\phi} + g\eta^2) dx$) in a long time forth-and-back
 407 simulation. The forward simulation is carried out up to $t = 10^3 T_0$, where T_0 is the period of the Stokes
 408 wave. Then, the time is reversed and the backward simulation is performed down to the initial time

409 $t = 0$. Simulations are done with different values of the tolerance parameter TOL and the parameter
410 $ITER$.

411 Fig. 1 presents the results of these simulations. In Fig. 1(a), the free surface elevation is plotted at $t = 0$,
412 $t = 10^3 T_0$ and $t = 0$ (after backward simulation), computed with $TOL = 10^{-8}$ and $ITER = 3$. The effect of the
413 parameters TOL and $ITER$ on the convergence of the model are depicted Fig. 1(b) and (c), respectively. The
414 evolution of the total energy (with $TOL = 10^{-8}$ and $ITER = 3$) is shown in Fig. 1(d). The results in Fig. 1
415 motivate for the following comments:

- 416 (i) The method converges quickly with the number of iterations, $ITER$. Although there are substantial dif-
417 ferences (after long time) between one and three iterations, more than three iterations do not provide
418 further improvements. For very accurate long time simulations it is therefore sufficient to employ
419 $ITER = 3$. For short simulations, one iteration is sufficient, most of the time, however.
- 420 (ii) The reversibility of the scheme increases as the tolerance parameter TOL decreases. With $TOL = 10^{-8}$
421 (at least for this particular long time forward–backward simulation) the initial condition is perfectly
422 recovered (Fig. 1(a) and (b)). This means that the errors due to the temporal integrator, to the evalu-
423 ation of the Green integral and the accumulation of round-off errors are insignificant.
- 424 (iii) The total energy is relatively well conserved (Fig. 1(d)) and, more importantly, no increasing or
425 decreasing trend is observed. The absence of a trend is crucial for the reversibility of the scheme.
426 The integrator used is an explicit Runge–Kutta scheme, and one may expect the total energy to
427 increase during the simulation, however. Such a global trend is observed in long time simulations if
428 $TOL = 10^{-6}$ is used (results not shown here). Setting $TOL = 10^{-8}$ reduces an increase in the total energy
429 error to a very low value. Even after 2000 periods of propagation, we do not observe any trend. On the
430 other hand, usual smoothing techniques or filtering decreases the total energy, often in a dramatic way.
431 Since neither smoothing nor filtering is used here, the total energy is allowed to be conserved. With no
432 smoothing techniques used, one could then expect high frequencies of the numerical solution to blow-
433 up. Indeed the long time simulations for large waves show that the scheme is highly stable.
- 434 (iv) The phase shift error obtained from the numerical solution is only of about 18° after 1000 periods of
435 propagation (Fig. 1(a) and (b)). This demonstrates the efficiency of the evaluation procedure of V .

436 To further check the convergence of the method, we perform a series of simulations where we fix
437 $TOL = 10^{-8}$ and $ITER = 3$, varying the number of collocation nodes in both directions. All the simulations
438 are carried out from $t = 0$ up to $t = 10^3 T_0$. We evaluate, during each simulation, the relative error in the
439 effective period (or alternatively the small phase shift) as compared to the period of the Stokes wave T_0 .
440 The relative error (in percents) is $\varepsilon_{err} = 100|T - T_0|/T_0$ where $T = 2\pi/\omega$ denotes the effective period. Here
441 ω is evaluated numerically from the phase shift by $\omega t = \omega_0 t + \Delta\varphi$ where $\Delta\varphi$ is given in radians at
442 $t = mT_0$ and where $\omega_0 = 2\pi/T_0$. Table 1 presents the relative error for several resolutions. It can be seen
443 from these examples that the method converges quickly with increasing number of nodes in both directions.
444 For the simulations corresponding to a purely two-dimensional problem, the strong contribution to an en-
445 hanced accuracy due to a refinement in the lateral direction, increasing the value of N_2 , may seem surpris-
446 ing. This is due to the fact that the evaluation of the local integrals are performed in both directions,
447 however. It can be noted that the simulations with a discretization of 64×128 collocation points lead to
448 a very small relative error in the period (see Table 1). The phase shift error obtained in this case is only
449 of about one third of a degree after 1000 periods of propagation.

451 4.2. Progressive solitary wave

452 To further illustrate the efficiency of the method, we consider as well a problem in shallow water. A sol-
453 itary wave is propagated along the numerical tank in a forward time simulation. Then the simulation is

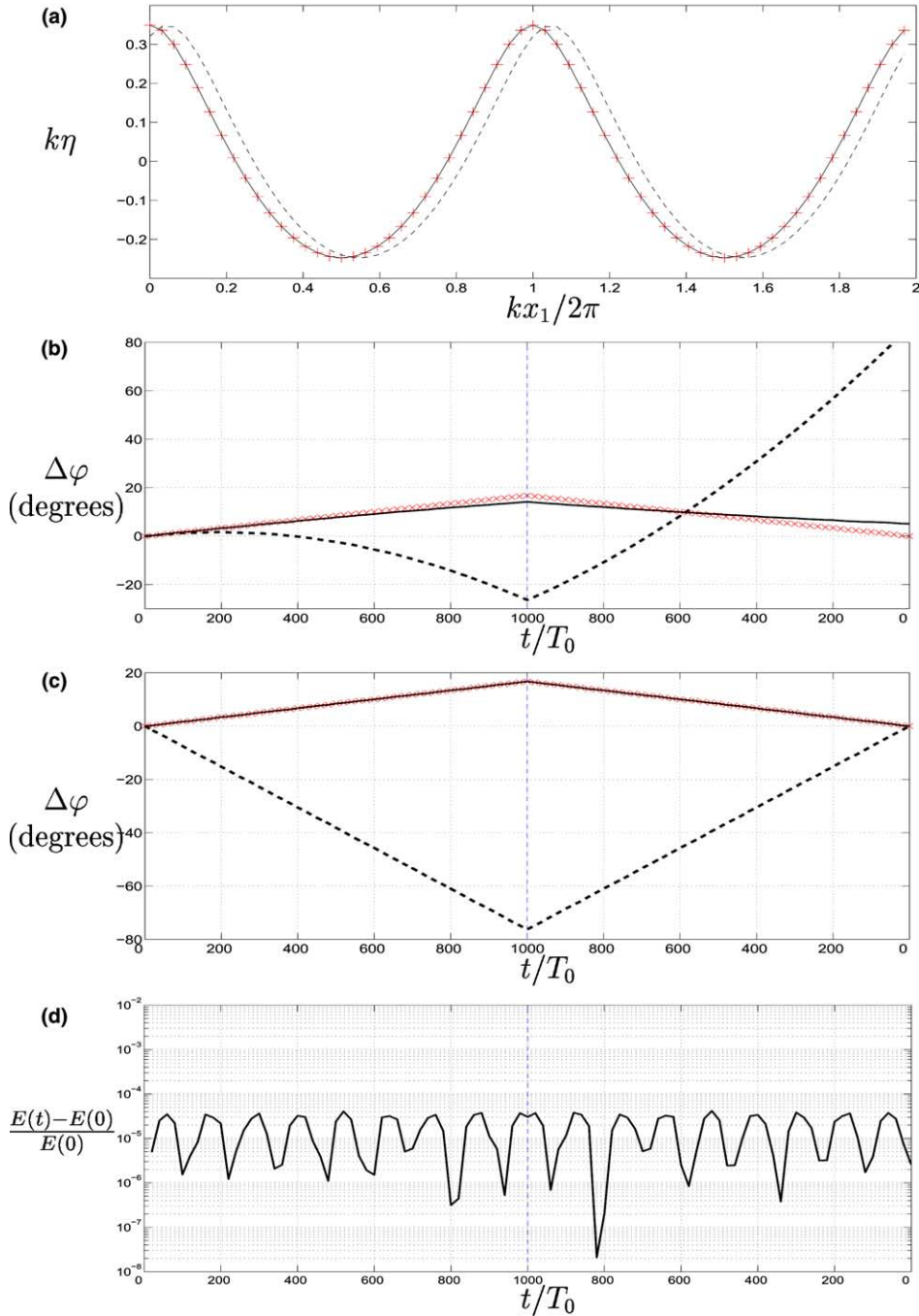


Fig. 1. Forward-backward simulation of a Stokes wave ($ak = 0.2985$) discretized over 64×64 collocation points. (a) Surface at: (—) $t = 0$, (---) $t = 10^3 T_0$, (+) $t = 0$ (after backward integration in time); ($\text{TOL} = 10^{-8}$, $\text{ITER} = 3$). (b) Evolution of phase error $\Delta\varphi$ with $\text{ITER} = 3$ and (---) $\text{TOL} = 10^{-6}$, (—) $\text{TOL} = 10^{-7}$, (\times) $\text{TOL} = 10^{-8}$. (c) Evolution of the phase error $\Delta\varphi$ with $\text{TOL} = 10^{-8}$ and (---) $\text{ITER} = 1$, (—) $\text{ITER} = 3$, (\times) $\text{ITER} = 5$. (d) Relative error of the total energy ($\text{TOL} = 10^{-8}$, $\text{ITER} = 3$).

Table 1

Relative error (percent) of the wave period $\varepsilon_{\text{err}} = 100|T - T_0|/T_0$ computed for a Stokes wave $ak = 0.2985$

$N_2 + N_2$	$N_1 + N_1$			
	16	32	64	256
16	4.1958	0.1509	0.0234	0.0238
32	4.2035	0.1650	0.0115	0.0116
64	4.2044	0.1752	0.0046	0.0058
128	4.2044	0.1747	0.0001	0.0001

The computational domain includes two wavelengths in each direction and is discretized over $2N_1 \times 2N_2$ collocation points. T_0 corresponds to the exact wave period computed from [14]. The simulated wave period T is evaluated from the obtained phase shift after $1000T_0$ of propagation. Using $\text{ITER} = 3$ and $\text{ToL} = 10^{-8}$. A relative error of 0.0001% corresponds to about 0.3° phase shift after 1000 periods of propagation.

454 reversed, as in the previous example. For illustration, we consider a solitary wave with $ah/h = 0.6$ (a denotes
 455 the maximal excursion of the wave, h the water depth). The initial condition is obtained using an algorithm
 456 by Tanaka [32] which computes the exact solitary wave solution. The solitary wave is discretized over
 457 (4096×32) collocation points, with $\Delta x_1/h = 0.2$ and $\Delta x_2/h = 0.3$. Fig. 2 presents the time evolution of the
 458 free surface elevation while the Fig. 3 compares the elevation at $t = 0$, $t = 250\sqrt{h/g}$ and after backward
 459 integration in time. Here the numerical parameters have been taken as $\lambda/h = (10, 10)$, $\text{ToL} = 10^{-7}$ and
 460 $\text{ITER} = 3$. The initial condition is recovered after backward integration in time, similarly to the previous
 461 example (Fig. 3).

462 These two examples illustrate the efficiency of the method. Considering two-dimensional exact solutions
 463 in infinite depth and in shallow water, we show that the time integration scheme is very efficient while the
 464 obtained solution is very accurate. Owing to the use of fast algorithm for the evaluation of Discrete Fourier
 465 Transform, the scheme is very fast while the anti-aliasing technique allows us to avoid the use of smoothing.
 466 This leads to computations where, even on very long time simulations, the total energy is conserved. The
 467 solution is accurate and the computation is stable.

468 4.3. Crescent wave patterns

469 While the physics in the previous examples were purely two-dimensional, we now illustrate the potential
 470 of the method computing three-dimensional instabilities of Stokes waves. We study the evolution of large
 471 amplitude Stokes waves perturbed by a small initial three-dimensional perturbation. We focus on the emer-
 472 gence of crescent wave patterns due to class II instabilities (following McLean's description [24]). The evo-
 473 lution of such class II instabilities have been the topic of many studies. Experimental investigations [29,25]
 474 as well as theoretical [28] and numerical ones [38] provide a good understanding of the underlying phenom-
 475 enon responsible for the formation of crescent wave patterns. Two satellites of wavevectors \mathbf{k}_a and \mathbf{k}_b and
 476 respective frequencies ω_a and ω_b , may get into resonance with the fundamental of the Stokes wave,
 477 $\mathbf{k}_0 = (1, 0)\mathbf{k}_0$ and frequency ω_0 , in a quintet interaction if the following resonance condition is fulfilled:

$$\begin{cases} \mathbf{k}_a + \mathbf{k}_b = 3\mathbf{k}_0, \\ \omega_a + \omega_b = 3\omega_0. \end{cases} \quad (26)$$

481 Let us consider an initial perturbation with dominant wavevectors $\mathbf{k}_a = (1 + p, q)\mathbf{k}_0$ and $\mathbf{k}_b = (2 - p, -q)\mathbf{k}_0$
 482 where p and q are arbitrary real numbers. If (p, q) lies in the class II instability zone, the quintet interaction
 483 (26) leads to the formation of crescent wave patterns. The most unstable perturbation of class II corre-
 484 sponds to $p = 1/2$. The corresponding pattern, known as horse-shoe pattern, is phase-locked to the unper-
 485 turbed Stokes waves. Many observations of such patterns have been reported while another interesting
 486 three-dimensional pattern was generated experimentally by Collard and Caulliez [7]. This pattern, named

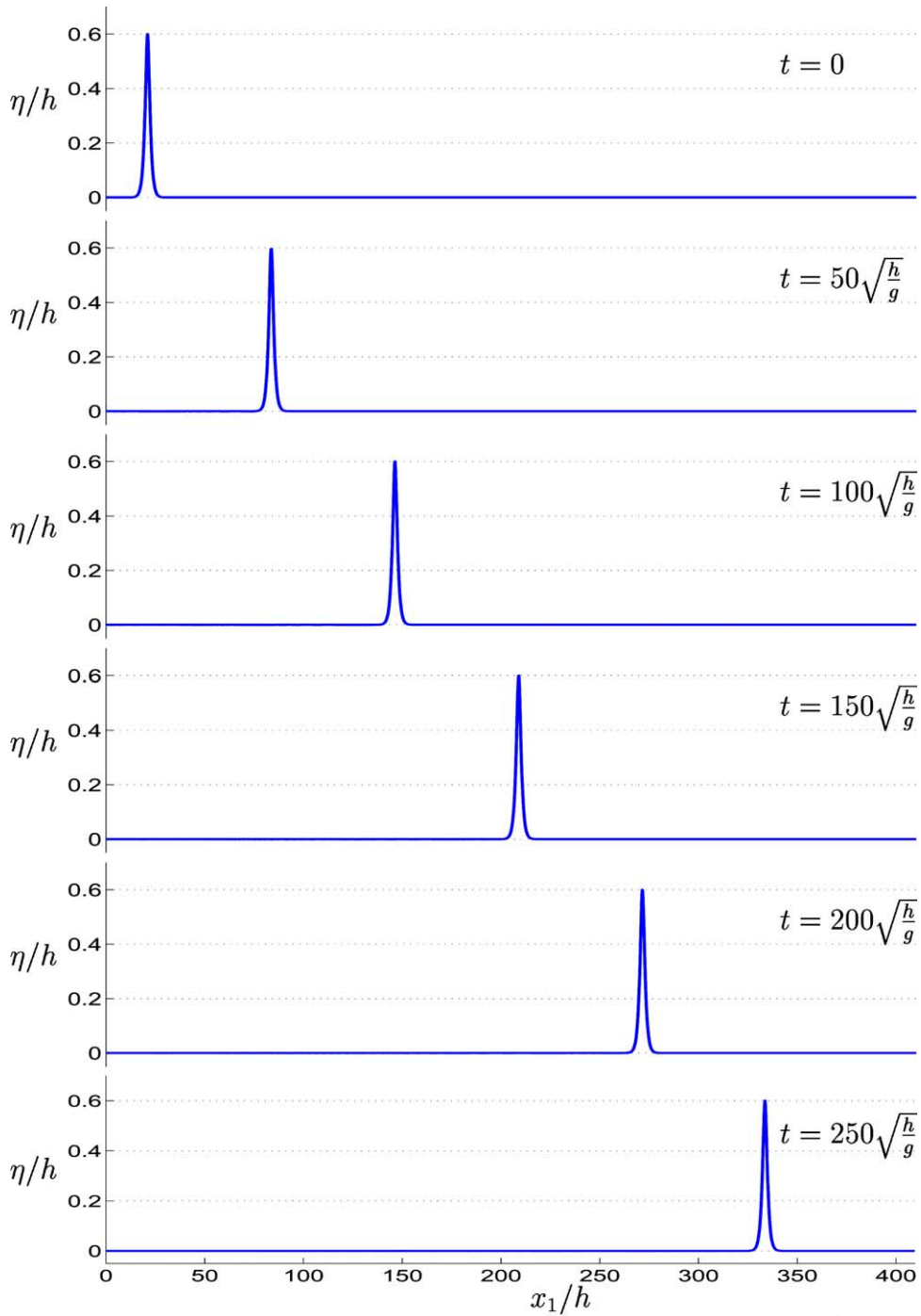


Fig. 2. Propagation of a solitary wave $ah = 0.6$ with $\text{TOL} = 10^{-7}$ and $\text{ITER} = 3$. Elevation at $t = \{0; 50; 100; 150; 200; 250\}\sqrt{h/g}$.

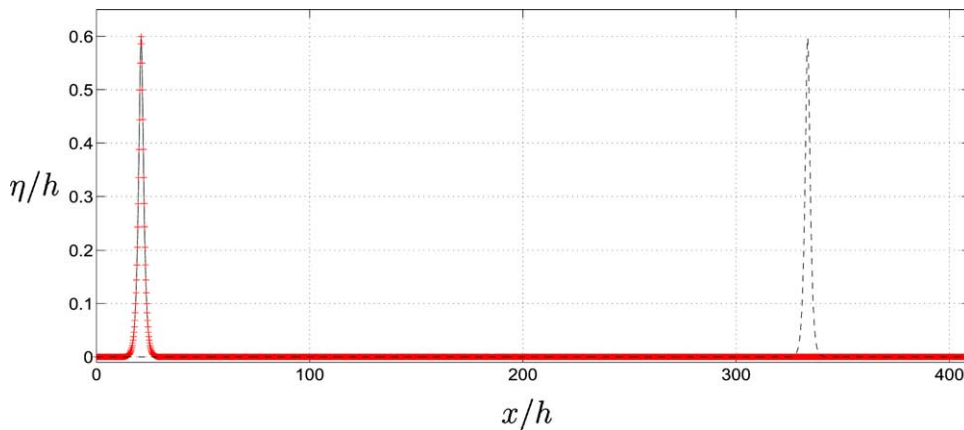


Fig. 3. Same as Fig. 2 in a simulation back and forth in time. Surface elevation at: $-t = 0$, $-t = 250\sqrt{h/g}$, $+t = 0$ (after backward integration in time).

487 oscillating horse-shoe pattern, corresponds to the development of the unstable mode at $p = 0$. The pattern
 488 was in the wave tank experiments caused by a perturbation that fits with the finite width of the tank.

489 In order to reproduce numerically such patterns with the present model, we compute first an exact
 490 numerical solution of plane Stokes waves of steepness $ak_0 = 0.2985$ [14]. A small perturbation η' of the wave
 491 surface, taking the form $\eta' = \varepsilon a \sin[(1+p)k_0 x_1] \cos(qk_0 x_2)$, is added to the Stokes wave train. Here, ε is a
 492 small number, making the amplitude of the initial perturbation field a fraction of the Stokes waves. For
 493 each simulation, four periods of Stokes waves in the longitudinal direction and three periods of the pertur-
 494 bation in the transversal direction are resolved by (128×64) nodes. The values of $(p, |q|)$ are chosen as
 495 $(0.5, 1.25)$ in the first simulation and as $(0, 1.32)$ and $(1, 1.32)$ in the second one. These choices correspond
 496 to unstable modes in the (p, q) -plane, according to the analysis of the Class II instability [24]. The corre-
 497 sponding wave vectors involved in (26) are then $\mathbf{k}_0 = (1, 0)k_0$, $\mathbf{k}_1 = (1.5, 1.25)k_0$ and $\mathbf{k}_1^* = (1.5, -1.25)k_0$ in
 498 the first simulation. Two quintets are involved in the second simulation: $\mathbf{k}_0, \mathbf{k}_2 = (1, 1.32)k_0$
 499 and $\mathbf{k}_3^* = (2, -1.32)$ for the first quintet and $\mathbf{k}_0, \mathbf{k}_3 = (2, 1.32)$, $\mathbf{k}_2^* = (1, -1.32)k_0$ for the second one. The
 500 growth of the crescent formed waves is then computed up to the level when breaking occurs in the simu-
 501 lations, corresponding to a saturation of the perturbations in real conditions like in a wave laboratory. We
 502 compare the simulated wave fields prior to breaking with observations that are available. It is noted that the
 503 present simulations differ from the physical laboratory experiments on a very important point: in the exper-
 504 iments the resonant quintets are balanced by the effect of breaking, preventing a further growth of the per-
 505 turbation waves, contributing to a steady state. The latter is not achieved by a conservative modeling.

506 The evolution of the modal energy for the wave vectors involved in the two simulations are presented
 507 Fig. 4.

508 Fig. 4(a) presents the results from the first simulation. The dynamics leads to the formation of horse-shoe
 509 patterns through the quintet interaction $\mathbf{k}_1 + \mathbf{k}_1^* = 3\mathbf{k}_0$.

510 Fig. 4(b) is concerned with the results from the second simulation. The dynamics leads to the formation
 511 of oscillating horse-shoe patterns. Here the two quintet interactions are $\mathbf{k}_2 + \mathbf{k}_3^* = 3\mathbf{k}_0$ and $\mathbf{k}_3 + \mathbf{k}_2^* = 3\mathbf{k}_0$.
 512 The continuous growth is accompanied by an oscillatory energy transfer between the modes (due to the
 513 resonant interaction $\mathbf{k}_2 + \mathbf{k}_3^* = \mathbf{k}_3 + \mathbf{k}_2^*$).

514 Fig. 5(a) and (b) presents the free surface elevation corresponding to horse-shoe and oscillating horse-
 515 shoe patterns, respectively, while Fig. 5(c) and (d) presents the corresponding wave frequency spectra.
 516 The superharmonic frequency peaks that appear in Fig. 5(c) and (d) confirms the second condition for
 517 the quintet interaction (26). While the peaks corresponding to $\omega_0, 2\omega_0, \dots$ are due to the basic Stokes wave,

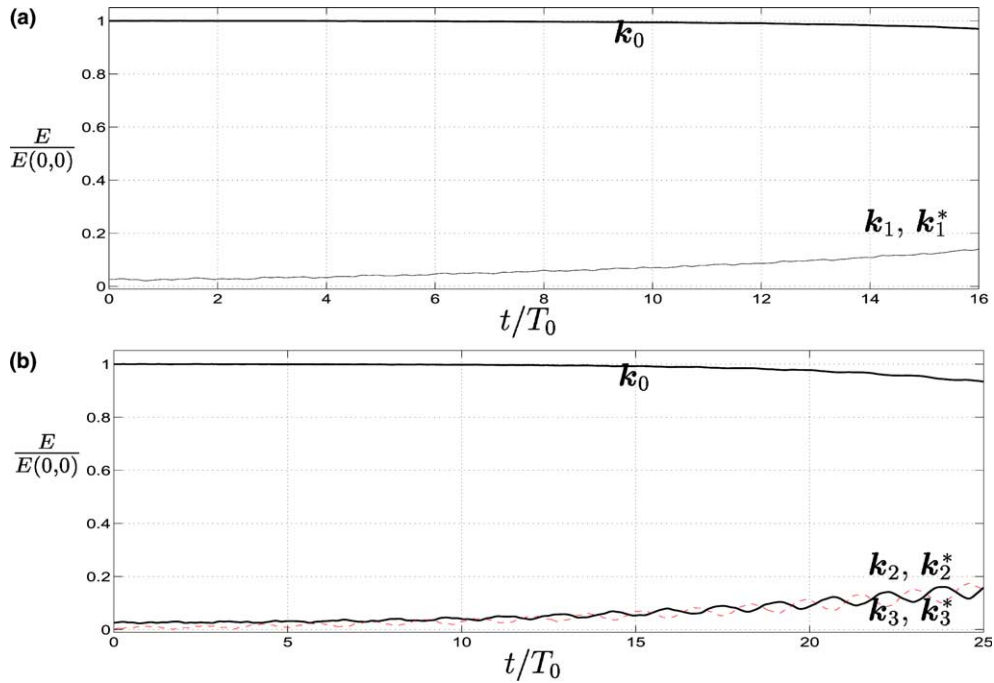


Fig. 4. Evolution of spectral energy for the main modes. (a) $k_0 = (1,0)$, $k_1 = (1.5, 1.25)$, $k_1^* = (1.5, -1.25)$. The initial wave field is a Stokes wave with $(ak)_0 = 0.3$ and the initial perturbations were set at k_1 and k_1^* with $\varepsilon = 0.025$. (b) $k_0 = (1,0)$, $k_2 = (1, 1.32)$, $k_2^* = (1, -1.32)$, $k_3 = (2, 1.32)$, $k_3^* = (2, -1.32)$. The initial wave field is a Stokes wave with $(ak)_0 = 0.3$ and the initial perturbations were set at k_2 and k_2^* with $\varepsilon = 0.025$.

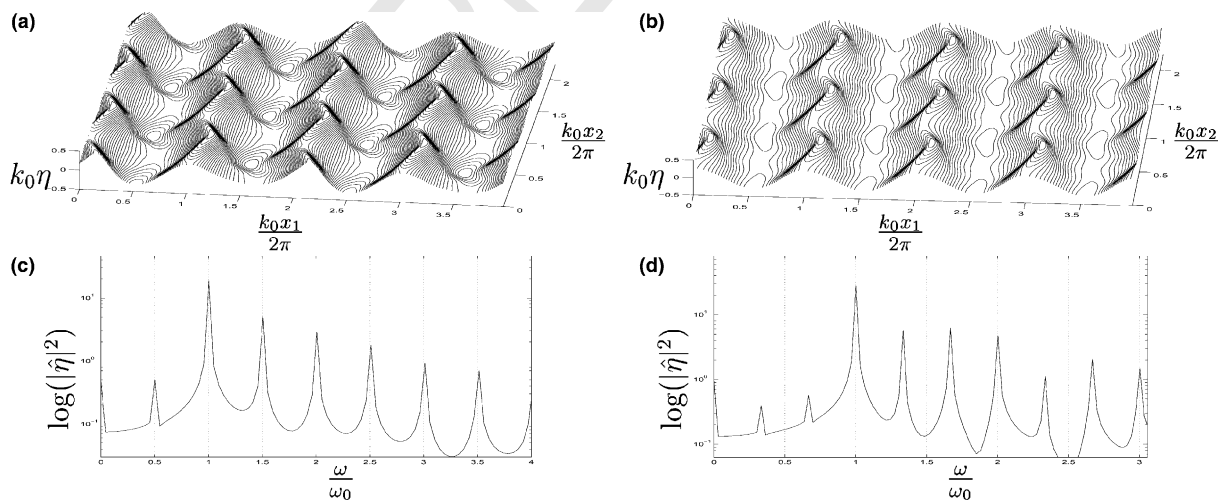


Fig. 5. Free surface elevation corresponding to (a) Fig. 4(a) at $t/T_0 = 16$ and (b) Fig. 4(b) at $t/T_0 = 23$. (c, d) Wave frequency spectra, (a, c) horse-shoe pattern, (b, d) oscillating horse-shoe.

518 additional ones at $1.5\omega_0, \dots$ (Fig. 5(c)) are due to k_1 and k_1^* while the peaks at $4/3\omega_0, 5/3\omega_0, \dots$ (Fig. 5(d))
 519 correspond to k_2, k_3, k_3^* and k_2^* .

520 For the sake of validation of the present results, a direct comparison with the experiments on the steady
 521 horse shoes are performed. Su [29] used five parameters to describe the waves (Fig. 6). Table 2 presents Su's
 522 results compared to the ones we obtained from the simulations just before breaking. Our results has a max-
 523 imum relative difference from the observations of less than one percent for four of the parameters and six
 524 percent for the remaining parameter. For comparison, the results from the numerical simulation of Xue
 525 et al. [38] have been added in Table 2. Their simulations differ from ours, however, in the sense that the
 526 initial level of disturbance was much higher in their simulations (they used $\varepsilon = 0.16$) and that they consid-
 527 ered slightly steeper initial Stokes waves ($ak = 0.33$) in their simulations. The agreement between the exper-
 528 imental results and the present numerical predictions is gratifying. This means that the final stage of the
 529 computed steady horse-shoe pattern corresponds to the experimentally observed one, both in amplitude
 530 and wave length.

531 Secondly, we perform comparisons with experimental results of Collard and Caulliez [7] for the oscillat-
 532 ing horse-shoe patterns. We consider first the experimental observations of the oscillatory horse-shoe pat-
 533 tern, at the stage where saturation is reached. The log-plot of the energy density shows a ratio between the
 534 perturbation modes and the fundamental being $\sim 1.5/3.5$ [7]. The corresponding result for the computations
 535 is $\sim 2/3.5$, see the Fig. 5(d). This means that the simulations of the oscillatory horse-shoe patterns are carried
 536 out up to a level corresponding to the experimental observations where a further growth of the waves is
 537 limited by wave breaking.

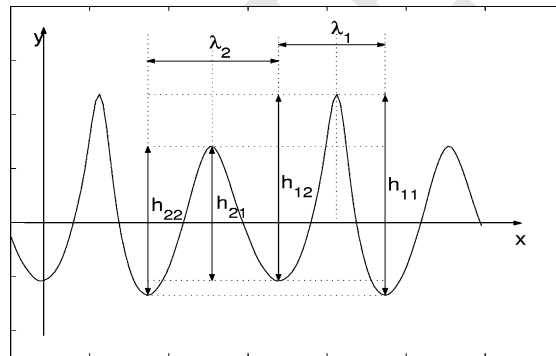


Fig. 6. Definition sketch of Su's geometrical parameters for the steady horse-shoe pattern. Wave elevation along propagation direction, through main (every second) maximum perturbation peak (see Fig. 5(a)).

Table 2

Comparison of characteristic crescent wave geometrical parameters for which quasi-steady state is assumed to be reached

	λ_1/λ_2	h_{11}/h_{12}	h_{21}/h_{22}	h_{11}/h_{21}	S_{\max}
Su [29]	1.28	1.10	0.88	1.66	0.65
Present model (Fig. 5(a))	1.28	1.11	0.88	1.56	0.66
Xue et al. [38] $t = t_1$	1.05	1.18	0.81	1.49	0.45
Xue et al. [38] $t = t_2$	1.07	1.09	0.88	1.64	0.64
Xue et al. [38] $t = t_3$	1.03	1.18	0.80	1.63	0.69
Xue et al. [38] $t = t_4$	1.17	1.26	0.75	1.60	0.51

$S_{\max} = \text{Max}(|\eta_x|)$ denotes the maximum slope.

538 For the results concerning the steady horse shoes, the computations were performed on a 1.3 GHz Pen-
539 tium 4M processor (laptop). The resolution was (128×64) nodes and the numerical parameters were taken
540 as $TOL = 10^{-7}$ and $ITER = 3$. The total computational time for each of these two simulations was ≈ 5500 s.

541 5. Concluding remarks

542 We have developed a numerical method to simulate fully nonlinear non-overturning free-surface waves.
543 The water depth is either finite or infinite. While other methods exist to solve this problem, they suffer from
544 several drawbacks. Numerical stability of the solution is usually a crucial point and is, in practice, a very
545 limiting factor. One has often to use smoothing techniques to avoid numerical blow-up of the solution.
546 Physically, this means that global parameters such as the total energy are not well conserved during sim-
547 ulations of wave field evolution. Moreover, numerous methods use expansion techniques about the free sur-
548 face level at rest. This implies limitation to small to moderate local steepnesses of the solution. Finally, the
549 time execution is as well a very limiting factor, making large scale simulations unrealistic.

550 The strategy we present here is based on an integral equation formulation and extensive use of Fourier
551 transform. At each step in the time integrator scheme, the Dirichlet to Neumann operator (solution of the
552 Laplace equation) is evaluated by expanding the operator through a highly truncated sum of convolution
553 terms, plus some integrals, representing the remainder in a perturbation expansion, with kernels that decay
554 quickly in space. The global convolution terms are computed very quickly via FFTs. The local contribu-
555 tions, due to the integrals, are evaluated by numerical integration over limited regions in the horizontal
556 plane. Moreover, the computation of the integrals (both global FFTs and local integrations) is, by essence,
557 easily parallelizable. This allows implementation on hybrid architectures and leads to very fast evaluation
558 of the local terms.

559 The Dirichlet to Neumann operator is evaluated by an iterative procedure that is rapidly converging. In
560 many applications one iteration is sufficient. In this case the inversion procedure of the Laplace equation is
561 explicit. The number of iterations is in the code governed by the parameter $ITER$. Very accurate predictions
562 are obtained using $ITER = 3$. This is important for long time simulations in large tanks. There is no gain in
563 using a higher value of $ITER$.

564 In order to limit the aliasing errors, the spectra are extended using zeros-padding. This rather expensive
565 procedure cannot be carried out indefinitely, however. It is here implemented for products that are up to the
566 fourth power. Extraction of more convolution terms from the integrals over the horizontal plane is theo-
567 retically possible. This leads to even faster decaying contributions of the remaining integrals. We find that
568 such a procedure is accompanied by increasing numerical instability, however. This is due to aliasing errors
569 from higher order nonlinear terms which are difficult to tackle in practical computations.

570 Analytical integration of the linear part of the prognostic equations means that this part of the solution
571 is obtained to machine precision. The remaining nonlinear part is integrated using a highly accurate time
572 integrator combined with a special step size control technique. This yields a very stable and accurate time
573 integration scheme. We illustrate in three examples that the method converges quickly and that the errors
574 due to the temporal integrator, to the evaluation of the Green integral and the accumulation of round-off
575 errors are insignificant. The method can cope with the description of very steep waves and requires no
576 smoothing. The total energy is perfectly conserved during the numerical simulations and the scheme is
577 shown to be stable and accurate, even for very long time simulations of very steep wave events.

578 Owing to the development of new technologies, including the democratization of 64 bits machines and
579 multi-processor architectures, the size of the numerical tank appears no longer as a drastic limitation.
580 Large computations in both time and space of fully nonlinear water waves are now possible. Simulations
581 of evolution of wave spectra or freak wave generation using the present model are realistic in the near
582 future.

583 The present model limits itself by the periodic wave tank. For many physical applications one has to
 584 consider a tank of infinite length. If one wants to simulate an infinite channel the present model has to
 585 be modified to include wave damping at the border of the tank. Fully nonlinear wave generation and wave
 586 absorption are described in the accompanying paper, part II [5].

587 6. Uncited references

588 [30,35,36].

589 Acknowledgements

590 This work was conducted under the Strategic University Programme ‘Modeling of currents and wave for
 591 sea structures’ and the BmatA-programme ‘Computational methods for stratified flows involving internal
 592 waves’, both funded by the Research Council of Norway.

593 Appendix A. Boundary integrals for the bottom

594 As for the surface integrals, the kernels of the contributions due to the bottom in (5) are partially
 595 expanded around $D_B = 0$ (i.e., around $\eta = 0$). We introduce $R_B^2 = R^2 + (2h)^2$, and the part of the
 596 kernel which is a polynomial in D_B reduces to convolutions and can be computed via Fourier
 597 transforms.

598 Thus, applying the Fourier transform of (5) and using the relation

$$\mathcal{F}\{R_B^{-1}\} = 2\pi e_h k^{-1} e^{-ik \cdot x'}, \quad e_h \equiv e^{-2kh}, \quad (\text{A.1})$$

601 one obtains after some algebra (see [17, Section 6.1])

$$\begin{aligned} \mathcal{F}(V) = & k \tanh(kh) \mathcal{F}(\tilde{\phi}) - k \tanh(kh) \mathcal{F}\{\eta V_1\} - i\mathbf{k} \cdot \mathcal{F}\{\eta \nabla \tilde{\phi}\} + kC_h[e_h \mathcal{F}(\eta(V - V_1))] \\ & + \mathcal{F}(\eta \mathcal{F}^{-1}[e_h \mathcal{F}(V - V_1)]) + kC_h[\mathcal{F}(T(\tilde{\phi}) + T_1(\tilde{\phi})) + \mathcal{F}(N(V) + N_1(V))], \end{aligned} \quad (\text{A.2})$$

605 where $V_1 = \mathcal{F}^{-1}[k \tanh(kh) \mathcal{F}(\tilde{\phi})]$, $C_h \equiv 1/(1 + e_h)$ and

$$T(\tilde{\phi}) = \frac{1}{2\pi} \int \tilde{\phi}' [1 - (1 + D^2)^{-3/2}] \nabla' \cdot \left[(\eta' - \eta) \nabla' \frac{1}{R} \right] dx', \quad (\text{A.3})$$

$$N(V) = \frac{1}{2\pi} \int \frac{V'}{R} [1 - (1 + D^2)^{-1/2}] dx', \quad (\text{A.4})$$

$$\begin{aligned} N(V) = & \frac{1}{2\pi} \int \frac{V'}{R} [1 - (1 + D^2)^{-1/2} - D^2/2] dx' - \frac{k}{2} \mathcal{F}(\eta^2 V) + \frac{1}{2} \mathcal{F}(2\eta \mathcal{F}^{-1}[k \mathcal{F}(\eta V)]) \\ & - \frac{1}{2} \mathcal{F}(\eta^2 \mathcal{F}^{-1}[k \mathcal{F}(V)]), \end{aligned} \quad (\text{A.5})$$

$$T_1(\tilde{\phi}) = -\frac{1}{2\pi} \int \tilde{\phi}' \frac{12h^2(\eta' + \eta)}{R_B^5} dx' + \frac{1}{2\pi} \int \tilde{\phi}' [\mathbf{R} \cdot \nabla' \eta' - (\eta' + \eta) - 2h] \left[\frac{1}{R_1^3} - \frac{1}{R_B^3} \right] dx', \quad (\text{A.6})$$

$$\begin{aligned}
T_1(\tilde{\phi}) = & -\frac{1}{2\pi} \int \tilde{\phi}' \left(\frac{280h^4}{R_B^2} - 30h^2 \right) \frac{(\eta' + \eta)^3}{R_B^7} \mathbf{d}\mathbf{x}' + \frac{1}{2\pi} \int \tilde{\phi}' [\mathbf{R} \cdot \nabla' \eta' - (\eta' + \eta) - 2h] \\
& \cdot \left[\frac{1}{r_1^3} - \frac{1}{R_B^3} + \frac{6h(\eta' + \eta)}{R_B^5} - \left(\frac{30h^2}{R_B^2} - \frac{3}{2} \right) \cdot \frac{(\eta' - \eta)^2}{R_B^5} \right] \mathbf{d}\mathbf{x}' + \frac{1}{2} e_h \mathbf{i}\mathbf{k} \cdot \mathcal{F}(\eta^2 \nabla \tilde{\phi}) \\
& + \frac{1}{2} \mathcal{F}(2\eta \mathcal{F}^{-1}[e_h \mathbf{i}\mathbf{k} \cdot \mathcal{F}(\eta \nabla \tilde{\phi})]) - \frac{1}{2} \mathcal{F}(\eta^2 \mathcal{F}^{-1}[e_h k^2 \mathcal{F}(\tilde{\phi})]) - \frac{1}{6} e_h \mathbf{k}\mathbf{i}\mathbf{k} \cdot \mathcal{F}(\eta^3 \nabla \tilde{\phi}) \\
& - \frac{1}{6} \mathcal{F}(3\eta \mathcal{F}^{-1}[e_h \mathbf{k}\mathbf{i}\mathbf{k} \cdot \mathcal{F}(\eta^2 \nabla \tilde{\phi})]) - \frac{1}{6} \mathcal{F}(3\eta^2 \mathcal{F}^{-1}[e_h \mathbf{k}\mathbf{i}\mathbf{k} \cdot \mathcal{F}(\eta \nabla \tilde{\phi})]) \\
& + \frac{1}{6} \mathcal{F}(\eta^3 \mathcal{F}^{-1}[e_h k^3 \mathcal{F}(\tilde{\phi})]), \tag{A.7}
\end{aligned}$$

$$N_1(V) = \frac{1}{2\pi} \int V' \left(\frac{1}{R_B} - \frac{2h(\eta' + \eta)}{R_B^3} - \frac{1}{r_1} \right) \mathbf{d}\mathbf{x}', \tag{A.8}$$

$$\begin{aligned}
N_1(V) = & \frac{1}{2\pi} \int V' \left(\frac{1}{R_B} - \frac{2h(\eta' + \eta)}{R_B^3} - \frac{1}{r_1} \right) \mathbf{d}\mathbf{x}' + \frac{1}{2\pi} \int V' \left(\left(\frac{6h^2}{R_B^2} - \frac{1}{2} \right) \frac{(\eta' + \eta)^2}{R_B^3} - \left(\frac{20h^3}{R_B^2} - 3h \right) \frac{(\eta' + \eta)^3}{R_B^5} \right) \mathbf{d}\mathbf{x}' \\
& - \frac{k}{2} e_h \mathcal{F}(\eta^2 V) - \frac{1}{2} \mathcal{F}(2\eta \mathcal{F}^{-1}[k e_h \mathcal{F}(\eta V)]) - \frac{1}{2} \mathcal{F}(\eta^2 \mathcal{F}^{-1}[k e_h \mathcal{F}(V)]) + \frac{1}{6} e_h k^2 \mathcal{F}(\eta^3 V) \\
& + \frac{1}{6} \mathcal{F}(3\eta \mathcal{F}^{-1}[e_h k^2 \mathcal{F}(\eta^2 V)]) + \frac{1}{6} \mathcal{F}(3\eta^2 \mathcal{F}^{-1}[e_h k^2 \mathcal{F}(\eta V)]) + \frac{1}{6} \mathcal{F}(\eta^3 \mathcal{F}^{-1}[e_h k^2 \mathcal{F}(V)]) \tag{A.9}
\end{aligned}$$

627 Eqs. (A.2)–(A.4), (A.6) and (A.8) are equal to the single layer special case of the transient interface equa-
628 tions in Grue [17]. Eqs. (A.5), (A.7) and (A.9) are results of further expansions, and it is these versions
629 which are implemented. The surface integral involving $\tilde{\phi}$ can be expanded in even orders in nonlinearity.
630 If expanded to sixth order, the fourth order convolution term is unstable. Therefore, this integral is given
631 above to fourth order. The surface integral involving V can be expanded in odd orders. The cubic convo-
632 lution terms is usually stable, hence this integral is given above as fifth order. Each of the bottom integrals
633 are expanded in both even and odd orders in nonlinearity (i.e., 1, 2, 3, ...). Their fourth order convolution
634 terms are found to be stable, hence the integrals are given above as fifth order. The bottom integrals could
635 probably be expanded even further without the convolution terms becoming unstable.

636 The factor $e_h \equiv e^{-2kh}$ which appears in most convolution terms is numerically fortunate since it acts like a
637 low-pass filter, allowing even the quartic (and probably higher order) convolutions to be unhampered by
638 high-frequency noise.

639 References

- 640 [1] J.T. Beale, A convergent boundary integral method for three-dimensional water waves, *Math. Comp.* 70 (235) (2001) 977–1029.
641 [2] T.B. Benjamin, J.E. Feir, The disintegration of wave trains on deep water, *J. Fluid Mech.* 27 (1967) 417–430.
642 [3] J.P. Boyd, *Chebyshev and Fourier Spectral Methods*, Dover, New York, 2004.
643 [4] C. Canuto, M.Y. Haussaini, A. Quarteroni, T.A. Zang, *Spectral Methods in Fluid Dynamics*. Springer Series in Computational
644 Physics, Springer-Verlag, Berlin, 1987.
645 [5] D. Clamond, D. Fructus, J. Grue, Ø. Kristiansen, An efficient model for three-dimensional surface wave simulations. Part II:
646 Generation and absorption, *J. Comp. Phys.* (in press).
647 [6] D. Clamond, J. Grue, A fast method for fully nonlinear water wave computations, *J. Fluid Mech.* 447 (2001) 337–355.
648 [7] F. Collard, G. Caulliez, Oscillating crescent-shaped water wave patterns, *Phys. Fluid Lett.* 11 (1999) 3195–3197.
649 [8] W. Craig, C. Sulem, Numerical simulation of gravity waves, *J. Comp. Phys.* 108 (1993) 73–83.
650 [9] F. Dias, C. Kharif, Nonlinear gravity and capillary-gravity waves, *Annu. Rev. Fluid Mech.* 31 (1999) 301–346.

- 651 [10] J.W. Dold, D.H. Peregrine, Water-wave modulation, in: Proceedings of the 20th International Conference on Coastal
652 Engineering, American Society of Civil Engineers, Taipei, 10–14 November 1986, pp. 163–175.
- 653 [11] D. Dommermuth, D.K.P. Yue, A high-order spectral method for the study of nonlinear gravity waves, *J. Fluid Mech.* 184 (1987)
654 267–288.
- 655 [12] K.B. Dysthe, Note on a modification to the nonlinear Schrödinger equation for application to deep water, *Proc. R. Soc. Lond. A*
656 369 (1979) 105–114.
- 657 [13] K.B. Dysthe, K. Trulsen, H.E. Krogstad, H. Socquet-Juglard, Evolution of a narrow-band spectrum of random surface gravity
658 waves, *J. Fluid Mech.* 478 (2003) 1–10.
- 659 [14] J.D. Fenton, The numerical solution of steady water wave problems, *Comp. Geosci.* 14 (3) (1988) 357–368.
- 660 [15] J.D. Fenton, Numerical methods for nonlinear waves *Advances in Coastal and Ocean Engineering*, vol. 5, World Scientific,
661 Singapore, 1999, pp. 241–324.
- 662 [16] M. Francius, C. Kharif, On the disappearance of the lowest-order instability for steep gravity waves in finite depth, *Phys. Fluids* 15
663 (in press).
- 664 [17] J. Grue, On four highly nonlinear phenomena in wave theory and marine hydrodynamics, *Appl. Ocean Res.* 24 (2002) 261–274.
- 665 [18] E. Hairer, G. Wanner, Solving ordinary differential equations II. Stiff and differential-algebraic problems *Springer Series in*
666 *Computational Mathematics*, vol. 14, Springer-Verlag, Berlin, 1991.
- 667 [19] T.Y. Hou, P. Zhang, Convergence of a boundary integral method for 3D water waves, *Discrete Contin. Dyn. Syst. Ser. B* 2 (1)
668 (2002) 1–34.
- 669 [20] ISSC 2000, Report of the Environment Committee, in: 14th International Ship and Offshore Structures Congress, Nagasaki,
670 Japan.
- 671 [21] P.A.E.M. Janssen, Nonlinear four-wave interactions and freak waves, *J. Phys. Oceanogr.* 33 (2003) 863–884.
- 672 [22] C. Kharif, E. Pelinovsky, T. Talipova, A. Slunyaev, Focusing of nonlinear wave groups in deep water, *JETP Lett.* 73 (2001) 170–
673 175.
- 674 [23] M.S. Longuet-Higgins, E.D. Cokelet, The deformation of steep surface waves on water I. A numerical method of computation,
675 *Proc. R. Soc. Lond. A* 350 (1976) 1–26.
- 676 [24] J.W. McLean, Instability of finite amplitude water waves, *J. Fluid Mech.* 114 (1982) 315–330.
- 677 [25] W.K. Melville, The instability and breaking of deep-water waves, *J. Fluid Mech.* 115 (1982) 165–185.
- 678 [26] D.P. Nicholls, F. Reitich, Stability of high-order perturbative methods for the computation of Dirichlet–Neumann operators, *J.*
679 *Comput. Phys.* 170 (1) (2001) 276–298.
- 680 [27] M. Onorato, A.R. Osborne, M. Serio, Extreme wave events in directional, random oceanic sea states, *Phys. Fluid* 14 (2002) 25–28.
- 681 [28] V.I. Shrira, S.I. Badulin, C. Kharif, A model of water wave ‘horse-shoe’ patterns, *J. Fluid Mech.* 318 (1996) 375–404.
- 682 [29] M.Y. Su, Three-dimensional deep-water waves. Part 1. Experimental measurement of skew and symmetric wave patterns, *J. Fluid*
683 *Mech.* 124 (1982) 73–108.
- 684 [30] C. Sulem, C.P. Sulem, The nonlinear Schrödinger equation – self focusing and wave collapse *Applied Mathematical Sciences*, vol.
685 139, Springer, Berlin, 1999.
- 686 [31] C. Skandrani, C. Kharif, J. Poitevin, Nonlinear evolution of water surface waves: the frequency down-shift phenomenon,
687 *Comtemp. Math.* 200 (1996) 157–171.
- 688 [32] M. Tanaka, The stability of solitary waves, *Phys. Fluids* 29 (1986) 650–655.
- 689 [33] K. Trulsen, I. Kliakhadler, K.B. Dysthe, M.G. Velarde, On weakly nonlinear modulation of waves on deep water, *Phys. Fluids* 12
690 (10) (2000) 2432–2437.
- 691 [34] W.T. Tsai, D.K.P. Yue, Computation of nonlinear free-surface flows, *Annu. Rev. Fluid Mech.* 28 (1996) 249–278.
- 692 [35] J.V. Wehausen, E.V. Laitone, Surface waves, *Handbuch der Physik*, vol. 9 (3), Springer-Verlag, Berlin, 1960, pp. 446–778.
- 693 [36] B.J. West, Deep water gravity waves *Lecture Notes in Physics*, vol. 146, Springer Verlag, Berlin, 1981.
- 694 [37] B.J. West, K.A. Brueckner, R.S. Janda, D.M. Milder, R.L. Milton, A new numerical method for surface hydrodynamics, *J.*
695 *Geophys. Res.* 92 (11) (1987) 11803–11824.
- 696 [38] M. Xue, H. Xü, Y. Liu, D.K.P. Yue, Computations of fully nonlinear three-dimensional wave–wave and wave–body interactions.
697 Part 1. Dynamics of steep three-dimensional waves, *J. Fluid Mech.* 438 (2001) 11–39.
- 698 [39] H.C. Yuen, B.M. Lake, Nonlinear dynamics of deep-water gravity waves, *Adv. Appl. Mech.* 22 (1982) 67–229.
- 699 [40] V.E. Zakharov, Stability of periodic wave of finite amplitude on the surface of a deep fluid, *J. Appl. Mech. Phys., Engl. Transl.* 2
700 (1968) 190–198.
- 701